

TumorFlow: Physics-Guided Longitudinal MRI Synthesis of Glioblastoma Growth

Valentin Biller^{1*}, Niklas Bubeck^{1,2*}, Lucas Zimmer¹, Ayhan Can Erdur¹, Sandeep Nagar¹, Anke Meyer-Baese⁵, Daniel Rückert^{1,2,4}, Benedikt Wiestler^{1,2,3**}, and Jonas Weidner^{1,2**}

¹ Technical University of Munich, Germany.

² Munich Center for Machine Learning (MCML)

³ Dept. of Neuroradiology, Klinikum Rechts der Isar, Munich, Germany.

⁴ Imperial College London

⁵ Florida State University

* equal contribution

** equal contribution

{valentin.biller, niklas.bubeck, j.weidner}@tum.de

Abstract. Glioblastoma exhibits diverse, infiltrative, and patient-specific growth patterns that are only partially visible on routine MRI, making it difficult to reliably assess true tumor extent and personalize treatment planning and follow-up. We present a biophysically-conditioned generative framework that synthesizes biologically realistic 3D brain MRI volumes from estimated, spatially continuous tumor-concentration fields. Our approach combines a generative model with tumor-infiltration maps that can be propagated through time using a biophysical growth model, enabling fine-grained control over tumor shape and growth while preserving patient anatomy. This enables us to synthesize consistent tumor growth trajectories directly in the space of real patients, providing interpretable, controllable estimation of tumor infiltration and progression beyond what is explicitly observed in imaging. We evaluate the framework on longitudinal glioblastoma cases and demonstrate that it can generate temporally coherent sequences with realistic changes in tumor appearance and surrounding tissue response. These results suggest that integrating mechanistic tumor growth priors with modern generative modeling can provide a practical tool for patient-specific progression visualization and for generating controlled synthetic data to support downstream neuro-oncology workflows. In longitudinal extrapolation, we achieve a consistent 75% Dice overlap with the biophysical model while maintaining a constant PSNR of 25 in the surrounding tissue. Our code is available at: <https://github.com/valentin-biller/lgm.git>

Keywords: Glioblastoma · Tumor Growth Modeling · Longitudinal Brain MRI Synthesis · Biophysical Conditioning

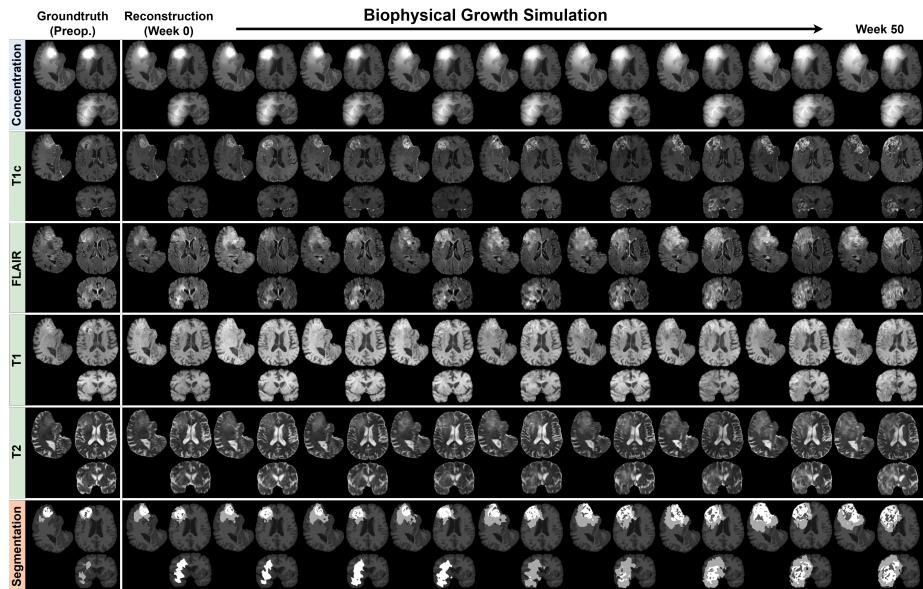


Fig. 1: **Representative longitudinal tumor growth prediction.** Starting from the preoperative state (week 0), a biophysical growth model is used to simulate time-resolved tumor concentration fields (blue), which serve as conditioning for image synthesis. The model generates T1c, FLAIR, T1, T2 modalities (green), preserving anatomy while capturing modality-specific progression. A standard segmentation model applied to the generated images yields time-consistent masks (orange).

1 Introduction

Glioblastoma is characterized by a highly irregular, infiltrative growth pattern. Magnetic resonance imaging (MRI) is essential for diagnosis, treatment planning, and longitudinal monitoring. However, routine MRI fails to detect the true extent and spread of glioblastoma and is, in particular, blind to the diffuse infiltration of tumor cells into the surrounding brain [24].

Biophysical brain tumor modeling has emerged as an interpretable and robust approach for estimating patient-specific tumor cell distributions and growth trajectories, enabling counterfactual predictions of tumor progression [12,2,22]. These models, however, typically operate on a continuous tumor-concentration field, which is disconnected from the imaging space used in clinical practice for decision-making.

Recently, generative models have emerged for brain tumor MRI [20,4,17,8]. However, they are conditioned on tumor segmentation masks, which constrain control to coarse morphology and prevent modeling spatially continuous infiltration patterns or their smooth evolution over time, a key requirement for *in silico* modeling of tumor response and personalized treatment decisions. In parallel,

methods that are conditioned only on tumor volume were developed [23,9,11]. These approaches aim to implicitly infer biophysical growth characteristics from data, but they often fail to produce temporally coherent progression and lack modifiability (e.g., for simulating different treatments). This limitation is further exacerbated by the scarcity and heterogeneity of longitudinal datasets.

To enable realistic, interpretable estimation of longitudinal disease progression, we combine, for the first time, a biophysical tumor growth model with high-fidelity MRI generation. Our main contributions are: **(i)** We train a generative flow matching model for 3D glioblastoma MRI on preoperative volumes only, which outperforms state-of-the-art approaches on image- and feature-level metrics. **(ii)** We condition the model on a tumor infiltration field, enabling fine-grained control over tumor generation significantly beyond what classical segmentation masks offer. **(iii)** We combine the generative model with state-of-the-art biophysical brain tumor modeling to generate robust and physically coherent longitudinal growth trajectories from cross-sectional MRI alone.

2 Method

We present a two-stage 3D latent generative framework in Fig. 2 for anatomically consistent brain tumor MRI synthesis and progression modeling. A pretrained 3D VAE encodes multimodal MR volumes, and a flow matching model in latent space conditions on modality, tissue segmentation, and biophysically-derived tumor-concentration fields. During inference, temporally propagated concentration maps enable biologically realistic tumor growth prediction.

Autoencoding. Let $\mathbf{x} \in \mathbb{R}^{256 \times 256 \times 160}$ denote a single-modality 3D MRI volume. We utilize a pretrained variational autoencoder (VAE) from the MAISI framework [7] which maps \mathbf{x} into latent space \mathbf{z} given the encoder \mathcal{E}_ϕ approximating the posterior distribution $q_\phi(z|x)$ with $z \sim \mathcal{N}(\mu_z, \Sigma_z)$ from which latent codes $\mathbf{z} \in \mathbb{R}^{4 \times 64 \times 64 \times 40}$ are sampled via the reparameterization trick. Afterwards, the image can be reconstructed again by estimating the likelihood $p_\theta(x|z)$ using the decoder \mathcal{D}_θ , where ϕ and θ are learnable parameters.

Latent Flow Matching. For generation, we utilize an Optimal Transport Flow Matching (OT-FM) formulation. Let \mathbf{z}_1 be a latent from a real MRI via the VAE encoder and $\mathbf{z}_0 \sim \mathcal{N}(\mathbf{0}, \mathbf{I})$ a Gaussian prior. We define an affine interpolation between source and target as $\mathbf{z}_\tau = (1 - \tau)\mathbf{z}_0 + \tau\mathbf{z}_1$ with $\tau \in [0, 1]$ and ground-truth velocity $\frac{d\mathbf{z}_\tau}{d\tau} = \mathbf{z}_1 - \mathbf{z}_0$. A neural network $v_\psi(\mathbf{z}_\tau, \tau, \mathbf{c})$ with learnable parameters ψ is conditioned on \mathbf{c} to predict the velocity field such that training minimizes

$$\mathcal{L}_{\text{FM}}(\psi) = \mathbb{E}_{\mathbf{z}_0, \mathbf{z}_1, \tau, \mathbf{c}} \left[\|v_\psi(\mathbf{z}_\tau, \tau, \mathbf{c}) - (\mathbf{z}_1 - \mathbf{z}_0)\|_2^2 \right], \quad \tau \sim \mathcal{U}[0, 1]. \quad (1)$$

At inference, a new sample $\hat{\mathbf{z}}_1$ can be generated by drawing from source and integrating over the learned velocity field. $\hat{\mathbf{z}}_1 = \mathbf{z}_0 + \int_0^1 v_\psi(\mathbf{z}_\tau, \tau, \mathbf{c}) d\tau$. The resulting latent $\hat{\mathbf{z}}_1$ is decoded by the VAE to reconstruct the final volume.

Conditioning. The conditioning input $\mathbf{c} = (m, \mathbf{c}_s, \mathbf{c}_{tc})$ comprises MRI modality m , tissue segmentation \mathbf{c}_s , and tumor concentration map \mathbf{c}_{tc} . The modality

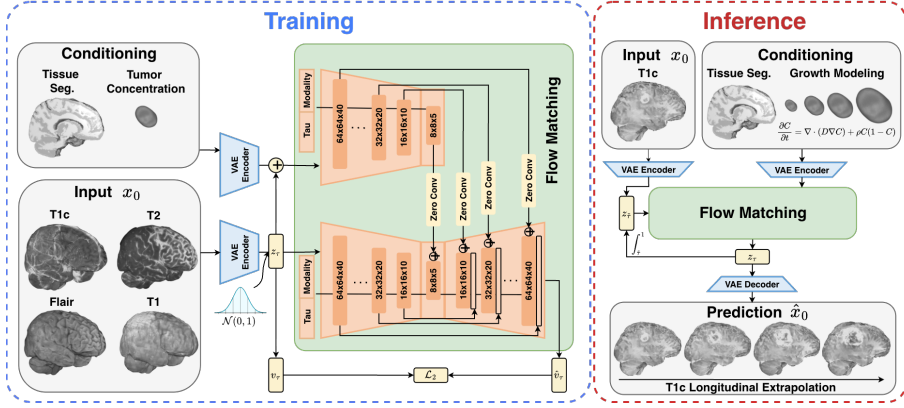


Fig. 2: **Architecture of TumorFlow.** Modality, tissue segmentations, and tumor concentrations are provided as conditioning inputs to the latent generative model. Orange boxes denote trainable modules, whereas blue boxes indicate frozen, pre-trained components. During inference, a full growth trajectory can be extrapolated from a biophysical simulation.

embedding $e_m = \text{Embed}(m)$ is concatenated with the timestep embedding. Both \mathbf{c}_s (from atlas registration) and \mathbf{c}_{tc} are encoded by the pretrained encoder \mathcal{E} , yielding $\mathbf{z}_s = \mathcal{E}(\mathbf{c}_s)$ and $\mathbf{z}_{tc} = \mathcal{E}(\mathbf{c}_{tc})$. Their concatenation forms the spatial conditioning tensor $\mathbf{c}_{\text{spatial}} = \text{concat}(\mathbf{z}_s, \mathbf{z}_{tc}) \in \mathbb{R}^{8 \times 64 \times 64 \times 40}$, which is injected into the U-Net backbone via a ControlNet-style branch [25]: $\mathbf{h}_\ell \leftarrow \mathbf{h}_\ell + \mathcal{F}_\ell(\mathbf{c}_{\text{spatial}})$, where \mathcal{F}_ℓ are learnable projections at scale ℓ .

Biophysical Tumor Growth Modeling. We model glioblastoma growth using the Fisher-Kolmogorov reaction-diffusion equation, which is widely adopted in the field [6,2,12]. It models the temporal change of the tumor concentration C based on a reaction and a diffusion term:

$$\frac{\partial C}{\partial t} = \nabla \cdot (D \nabla C) + \rho C (1 - C), \quad (2)$$

where D is a tissue-dependent diffusion coefficient, and ρ the proliferation rate.

Longitudinal Image Generation. Longitudinal generation must balance the temporal consistency of patient-specific anatomy with the need to reflect progressive tumor growth. Let $\{\mathbf{c}_{tc}^t\}_{t=0}^T$ denote time-indexed t tumor concentration fields. The initial concentration \mathbf{c}_{tc}^0 is estimated by a biophysical growth model [21] to fit the pre-op tumor segmentation. Each \mathbf{c}_{tc}^t is encoded into latent space and used for conditional synthesis. For temporal coherence and synthesis of time $t + 1$ the previous state z_1^t gets transported backward along the deterministic flow trajectory into a corrupted version z_τ^t . Given this intermediate representation, we then integrate forward under the updated conditioning,

Table 1: Quantitative evaluation of generated volumes. Dice compares thresholded tumor concentration fields with segmentations from a pretrained BraTS model. FID, KID, and MS-SSIM assess distributional alignment, perceptual similarity, and diversity against the test set. The reference metrics are empirical upper bounds derived from test-set calibration experiments, reflecting limits by VAE reconstruction fidelity, uncertainty in tumor-concentration derivations, and automatic tumor segmentation.

	Model	Dice \uparrow	FID \downarrow	KID \downarrow	MS-SSIM \uparrow
	Reference	0.779	0.330	0.001	–
<i>(Ours)</i> <i>Baseline</i>	TumorFlow	0.739	2.125	0.020	0.675
	Med-DDPM [4]	0.344	106.246	1.618	0.588
<i>Ablation</i>	OT-FM w. ViT	<u>0.572</u>	<u>2.540</u>	<u>0.026</u>	<u>0.675</u>
	DDPM w. U-Net	0.579	11.221	0.083	0.648

enabling controlled temporal evolution while preserving anatomical consistency:

$$\hat{\mathbf{z}}_1^{t+1} = \mathbf{z}_{\tilde{\tau}}^t + \int_{\tilde{\tau}}^1 v_{\psi}(\mathbf{z}_{\tau}^t, \tau, \mathbf{c}_{tc}^t) d\tau. \quad (3)$$

This scheme is recursively applied, yielding anatomically and temporally consistent longitudinal MRI synthesis. The corruption level $\tilde{\tau}$ is selected empirically for each method.

3 Experiments

Implementation Details. We use the publicly available BraTS 2021 dataset [1] and additional cohorts such as UCSF-PDGM [3], TCGA-GBM [15], TCGA-LGG [13], and Rembrandt [14], excluding overlapping patients. This aggregation increases distributional diversity [19] and mitigates memorization risk [18]. The combined dataset comprises 3,602 subjects, split into 80% training (2,881) and 20% validation (721). All volumes are co-registered to a common anatomical template, resampled to 1 mm³ isotropic resolution, and skull-stripped. For longitudinal evaluation, we include the Lumiere dataset [16]. Models are trained on a single NVIDIA A100 (40 GB) using AdamW (learning rate 10⁻⁴, zero weight decay) with cosine annealing and an EMA decay of $\gamma = 0.999$ for stability.

References, Baseline and Ablations Evaluation uses the held-out test set as a calibration baseline. Unless stated otherwise, Fréchet Inception Distance (FID) and Kernel Inception Distance (KID) are reported in units of $\times 10^{-3}$. Comparing reconstructions from the pretrained VAE yields PSNR 32.09 and FID/KID 0.330/0.001, establishing the empirical fidelity ceiling. For tumor modeling, Dice overlap between reconstructed concentration fields and MR-based automatic segmentations [10] reaches 0.779, reflecting the uncertainty-imposed upper bound on segmentation accuracy.

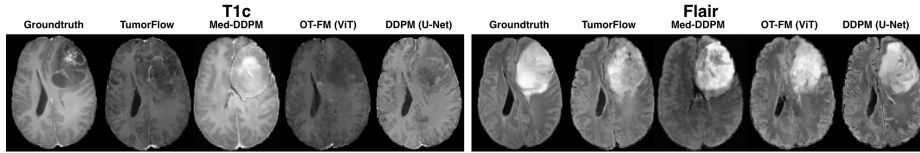


Fig. 3: **Qualitative Comparison.** Reconstructions from different methods.

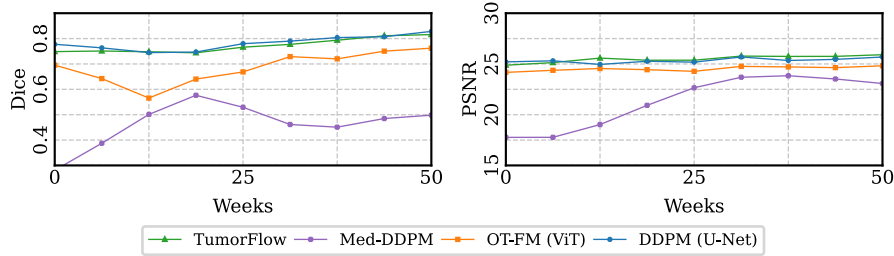


Fig. 4: **Left: Tumor Consistency.** Dice across time steps, assessing tumor growth consistency. **Right: Tissue Consistency.** PSNR across time steps measuring structural drift in healthy tissue. Stable values indicate coherent generation.

We compare against the BraTS-pretrained Med-DDPM baseline [4] by thresholding the grown tumor concentration map to obtain a segmentation mask for conditioning. Specifically, edema is assigned for concentration values in $[0.2, 0.6)$ and enhancing tumor for values ≥ 0.6 .

We further compare against two ablations: 1. switching the corruption paradigm to a Denoising Diffusion Probabilistic Model (DDPM), and 2. replacing the 3D U-Net backbone with a Vision Transformer (ViT) [5] using its base configuration and patch size of 2.

Generation of Static Brain Tumor MRI. We first assess the general *generative performance* of the model by evaluating image fidelity and diversity on the static, non-longitudinal setup. Specifically, we compute FID, KID, and MS-SSIM between the generated volumes and the real test volumes to quantify distributional fidelity and diversity of synthesized samples. Second, we evaluate *adherence* to the conditioning signal by comparing tumor volumes derived from the input concentration field and from the generated images. The reference volume is obtained by thresholding the concentration field at 0.2, which is the calibration threshold for the biophysical growth model. Tumor volumes in the synthesized images are estimated using an independent pretrained segmentation model within the BraTS Orchestrator [10], based on the top-performing method from the Adult Glioma Segmentation Challenge [1]. Adherence is quantified using the Dice Score [26] between the thresholded conditioning mask and the predicted segmentation.

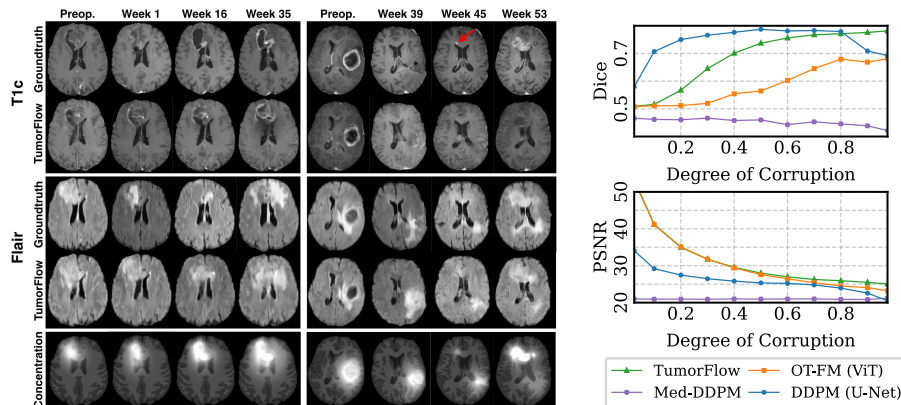


Fig. 5: **Left: Real patients.** Comparing TumorFlow and groundtruth tumor development in two patients from Lumiere [16]. The red arrow points to a new tumor lesion in the corpus callosum. **Right: Effect of corruption initialization on longitudinal generation.** Top: Dice between generated tumors and conditioning. Bottom: PSNR between consecutive non-tumorous regions.

Quantitative evaluation of fidelity, diversity, and conditioning adherence demonstrates that our model outperforms the Med-DDPM [4] baseline as well as the diffusion and ViT ablations in brain MRI synthesis (Table 1). Lower FID and KID scores indicate a closer match to real data, while higher MS-SSIM values confirm improved perceptual and structural fidelity. Overall, the Flow Matching formulation produces more realistic and anatomically consistent volumes than diffusion-based counterparts. Additionally, our model demonstrates substantially improved *tumor adherence* compared to the Med-DDPM [4] baseline, with generated tumor regions aligning more closely to the intended geometry, as shown qualitatively in Fig. 3. In particular, leveraging tumor concentration maps leads to higher Dice similarity between the target signal and the synthesized tumor, reflecting tighter spatial agreement.

Longitudinal Extrapolation. The TumorGrowthToolkit [2] is configured with proliferation rate $\rho = 0.03 \text{ d}^{-1}$ and diffusion coefficient $D = 0.28 \text{ mm}^2 \text{ d}^{-1}$ to generate physics-informed spatiotemporal tumor concentration fields $c^t(\mathbf{x})_{t=0}^T$, from which corresponding longitudinal MRI sequences are synthesized. *Temporal consistency* is enforced via predecessor-manipulation, where each time point is conditioned on the evolved concentration field and initialized at $\tilde{\tau} = 0.15$.

In Fig. 1, we show a representative longitudinal prediction over 50 weeks. The biophysical simulation produces a smooth tumor cell concentration trajectory that informs the generation of follow-up scans. Despite substantial changes in the extent of the tumor, the patient anatomy outside of the tumor remains stable over time. The growing tumor, in particular the necrotic and contrast-enhancing areas, exhibits realistic morphology and imaging characteristics. The

downstream segmentations provide an additional consistency check, producing masks that evolve plausibly and align well with the predicted growth pattern.

In the left panel of Fig. 4, *temporal consistency* of the simulated tumor progression is evaluated using the Dice score, where our model achieves the highest temporal stability, indicating that the evolving, synthetic tumors are highly realistic. On the right panel of that figure, temporal tissue consistency is quantified by computing pixel-wise fidelity in non-tumorous regions between consecutive time points. Structural drift in healthy tissue is measured by PSNR: excessively high values would indicate an overly static anatomy that impedes realistic tumor growth, while low values reflect excessive structural drift and diminished subject coherence over time. Our model achieves a balanced trade-off, maintaining stable Dice and PSNR curves that indicate temporally coherent synthesis. Over time, consistent metric values suggest controlled tumor progression and preserved anatomy, whereas deviations reveal either insufficient tumor growth dynamics or instability in structural tissue fidelity.

As treatment-naive longitudinal public data do not exist, we evaluate our method on the postoperative Lumiere Dataset (see Fig. 5 left). The images contain a resection cavity and post-surgery brain deformation, for which our model is not trained. We estimate tumor concentration by independently fitting a biophysical model at each time step. Generation is initialized from the pre-op image. Despite the resection cavity, we observe temporally consistent and anatomically plausible longitudinal images. In the right patient, we note a satellite lesion in the corpus callosum at week 45 (red arrow). We observe that this satellite lesion closely follows the predicted concentration growth pattern, while the surrounding anatomy remains visually consistent.

Ablation. In the stepwise corruption process of the optimal transport formulation, fine-grained features degrade earlier than coarse structures. To assess the impact of this, we evaluate our model and its variants across different architectures by varying the corruption level $\tilde{\tau}$ used to initialize the predecessor manipulation on the right panel of Fig. 5. Low $\tilde{\tau}$ values yield volumes nearly identical to the previous state, resulting in high PSNR but minimal tumor progression. Increasing $\tilde{\tau}$ induces stronger updates and more realistic growth dynamics. Our TumorFlow model exhibits a smooth, monotonic Dice response across corruption states, indicating stable and precise controllability of tumor evolution. In contrast, DDPM-based models exhibit irregular, less predictable trends, reflecting a weaker balance between anatomical stability and tumor fidelity. Med-DDPM [4] further deviates from the intended progression.

4 Conclusion

We introduced a physics-guided generative framework for longitudinal glioblastoma MRI synthesis that conditions high-fidelity 3D image generation on spatially continuous tumor concentration fields and evolves these fields over time with a Fisher-Kolmogorov reaction-diffusion growth model. By conditioning on spatially continuous tumor concentration fields and evolving them with a bio-

physical growth prior, we can generate follow-up images that reflect biologically plausible tumor growth trajectories while keeping the individual anatomy and image appearance stable over time. Importantly, we achieve this while training only on cross-sectional, preoperative data, effectively alleviating the persistent shortage of high-quality longitudinal datasets in medical imaging.

Future work will focus on more realistic modeling of tumor growth and treatment response, where our work lays an important foundation for *in silico* disease and treatment modeling.

References

1. Baid, U., Ghodasara, S., Mohan, S., Bilello, M., Calabrese, E., Colak, E., Farahani, K., Kalpathy-Cramer, J., Kitamura, F.C., Pati, S., et al.: The rsna-asnr-miccai brats 2021 benchmark on brain tumor segmentation and radiogenomic classification. arXiv preprint arXiv:2107.02314 (2021)
2. Balcerak, M., Weidner, J., Karnakov, P., Ezhov, I., Litvinov, S., Koumoutsakos, P., Amiranashvili, T., Zhang, R.Z., Lowengrub, J.S., Yakushev, I., et al.: Individualizing glioma radiotherapy planning by optimization of a data and physics-informed discrete loss. *Nature Communications* **16**(1), 5982 (2025)
3. Calabrese, E., Villanueva-Meyer, J.E., Rudie, J.D., Rauschecker, A.M., Baid, U., Bakas, S., Cha, S., Mongan, J.T., Hess, C.P.: The university of california san francisco preoperative diffuse glioma mri dataset. *Radiology: Artificial Intelligence* **4**(6), e220058 (2022)
4. Dorjsembe, Z., Pao, H.K., Odonchimed, S., Xiao, F.: Conditional diffusion models for semantic 3d brain mri synthesis. *IEEE Journal of Biomedical and Health Informatics* **28**(7), 4084–4093 (2024)
5. Dosovitskiy, A., Beyer, L., Kolesnikov, A., Weissenborn, D., Zhai, X., Unterthiner, T., Dehghani, M., Minderer, M., Heigold, G., Gelly, S., et al.: An image is worth 16x16 words: Transformers for image recognition at scale. arXiv preprint arXiv:2010.11929 (2020)
6. Ezhov, I., Scibilia, K., Franitza, K., Steinbauer, F., Shit, S., Zimmer, L., Lipkova, J., Kofler, F., Paetzold, J.C., Canalini, L., et al.: Learn-morph-infer: a new way of solving the inverse problem for brain tumor modeling. *Medical Image Analysis* **83**, 102672 (2023)
7. Guo, P., Zhao, C., Yang, D., Xu, Z., Nath, V., Tang, Y., Simon, B., Belue, M., Harmon, S., Turkbey, B., et al.: Maisi: Medical ai for synthetic imaging. In: 2025 IEEE/CVF Winter Conference on Applications of Computer Vision (WACV). pp. 4430–4441. IEEE (2025)
8. Jiang, L., Mao, Y., Wang, X., Chen, X., Li, C.: Cola-diff: Conditional latent diffusion model for multi-modal mri synthesis. In: International Conference on Medical Image Computing and Computer-Assisted Intervention. pp. 398–408. Springer (2023)
9. Kebaili, A., Lapuyade-Lahorgue, J., Vera, P., Ruan, S.: 3d mri synthesis with slice-based latent diffusion models: Improving tumor segmentation tasks in data-scarce regimes. In: 2024 IEEE International Symposium on Biomedical Imaging (ISBI). pp. 1–5. IEEE (2024)
10. Kofler, F., Rosier, M., Astaraki, M., Baid, U., Möller, H., Buchner, J.A., Steinbauer, F., Oswald, E., de la Rosa, E., Ezhov, I., et al.: Brats orchestrator: Democratizing and disseminating state-of-the-art brain tumor image analysis. arXiv preprint arXiv:2506.13807 (2025)
11. Laslo, D., Georgiou, E., Linguraru, M.G., Rauschecker, A., Muller, S., Jutzeler, C.R., Bruning, S.: Mechanistic learning with guided diffusion models to predict spatio-temporal brain tumor growth. arXiv preprint arXiv:2509.09610 (2025)
12. Lipkova, J., Angelikopoulos, P., Wu, S., Alberts, E., Wiestler, B., Diehl, C., Preibisch, C., Pyka, T., Combs, S.E., Hadjidakas, P., et al.: Personalized radiotherapy design for glioblastoma: integrating mathematical tumor models, multi-modal scans, and bayesian inference. *IEEE transactions on medical imaging* **38**(8), 1875–1884 (2019)

13. Pedano, N., Flanders, A.E., Scarpance, L., Mikkelsen, T., Eschbacher, J.M., Hermes, B., Sisneros, V., Barnholtz-Sloan, J., Ostrom, Q.: The cancer genome atlas low grade glioma collection (tcga-igg). (No Title) (2016)
14. Sayah, A., Bencheqroun, C., Bhuvaneshwar, K., Belouali, A., Bakas, S., Sako, C., Davatzikos, C., Alaoui, A., Madhavan, S., Gusev, Y.: Enhancing the rembrandt mri collection with expert segmentation labels and quantitative radiomic features. *Scientific Data* **9**(1), 338 (2022)
15. Scarpance, L., Mikkelsen, T., Cha, S., Rao, S., Tekchandani, S., Gutman, D., Saltz, J.H., Erickson, B.J., Pedano, N., Flanders, A.E., et al.: The cancer genome atlas glioblastoma multiforme collection (tcga-gbm). *The Cancer Imaging Archive* (2016)
16. Suter, Y., Knecht, U., Valenzuela, W., Notter, M., Hewer, E., Schucht, P., Wiest, R., Reyes, M.: The lumiere dataset: Longitudinal glioblastoma mri with expert rano evaluation. *Scientific data* **9**(1), 768 (2022)
17. Truong, N.C., Yogananda, C.G.B., Wagner, B.C., Holcomb, J.M., Reddy, D., Saadat, N., Hatanpaa, K.J., Patel, T.R., Fei, B., Lee, M.D., et al.: Synthesizing 3d multicontrast brain tumor mris using tumor mask conditioning. In: *Medical Imaging 2024: Imaging Informatics for Healthcare, Research, and Applications*. vol. 12931, pp. 116–120. SPIE (2024)
18. Usman Akbar, M., Larsson, M., Blystad, I., Eklund, A.: Brain tumor segmentation using synthetic mr images—a comparison of gans and diffusion models. *Scientific Data* **11**(1), 259 (2024)
19. Usman Akbar, M., Wang, W., Eklund, A.: Beware of diffusion models for synthesizing medical images—a comparison with gans in terms of memorizing brain mri and chest x-ray images. *Machine Learning: Science and Technology* **6**(1), 015022 (2025)
20. Wang, H., Liu, Z., Sun, K., Wang, X., Shen, D., Cui, Z.: 3d meddiffusion: A 3d medical latent diffusion model for controllable and high-quality medical image generation. *IEEE Transactions on Medical Imaging* (2025)
21. Weidner, J., Balcerak, M., Ezhov, I., Datchev, A., Lux, L., Rueckert, L.Z.D., Menze, B., Wiestler, B.: Spatial brain tumor concentration estimation for individualized radiotherapy planning. *arXiv e-prints* pp. arXiv–2412 (2024)
22. Weidner, J., Ezhov, I., Balcerak, M., Metz, M.C., Litvinov, S., Kaltenbach, S., Feiner, L., Lux, L., Kofler, F., Lipkova, J., et al.: A learnable prior improves inverse tumor growth modeling. *IEEE Transactions on Medical Imaging* **44**(3), 1297–1307 (2024)
23. Wolleb, J., Sandkühler, R., Bieder, F., Cattin, P.C.: The swiss army knife for image-to-image translation: Multi-task diffusion models. *arXiv preprint arXiv:2204.02641* (2022)
24. Yan, J.L., Li, C., Boonzaier, N.R., Fountain, D.M., Larkin, T.J., Matys, T., van der Hoorn, A., Price, S.J.: Multimodal mri characteristics of the glioblastoma infiltration beyond contrast enhancement. *Therapeutic advances in neurological disorders* **12**, 1756286419844664 (2019)
25. Zhang, L., Rao, A., Agrawala, M.: Adding conditional control to text-to-image diffusion models. In: *Proceedings of the IEEE/CVF international conference on computer vision*. pp. 3836–3847 (2023)
26. Zou, K.H., Warfield, S.K., Bharatha, A., Tempany, C.M., Kaus, M.R., Haker, S.J., Wells III, W.M., Jolesz, F.A., Kikinis, R.: Statistical validation of image segmentation quality based on a spatial overlap index1: scientific reports. *Academic radiology* **11**(2), 178–189 (2004)